Near-Field Effects on the in situ Estimation of Shear-Wave Velocity and Damping Ratio from MASW Tests

Near-field effects on the in-situ estimation of shear-wave velocity and damping ratio from MASW tests

Mauro Aimar[1], and Sebastiano Foti[2]

1: Assistant Professor, Department of Structural, Building and Geotechnical Engineering (DISEG), Politecnico di Torino, Corso Duca degli Abruzzi 24, 10129 Torino, Italy; email: mauro.aimar@polito.it (Corresponding author)

2: Full Professor, Department of Structural, Building and Geotechnical Engineering (DISEG), Politecnico di Torino, Corso Duca degli Abruzzi 24, 10129 Torino, Italy

Abstract

Multichannel Analysis of Surface Waves (MASW) is a viable approach for *in situ* estimation of shear wave velocity and damping ratio. However, conventional processing techniques assume that the recorded wavefield consists only of surface waves, and the presence of body waves leads to detrimental consequences on the reliability of the estimate, referred to as near-field effects. The latter typically induce oscillations in the estimated phase velocity at low frequencies, while little is known about their effect on phase attenuation. This study investigates the influence of near-field effects on the estimated phase velocity and phase attenuation on a synthetic dataset. The results show that the phase attenuation is far more sensitive to body waves than the phase velocity. Furthermore, the findings suggest that near-field effects can be mitigated by selecting the experimental data with Normalized Array Center Distance (NACD; i.e., the ratio between the average offset of the receivers and the Rayleigh wavelength) greater than 2-3. While phase velocity estimates are reliable at NACD values as low as 1, the requirement for NACD > 2-3 is mainly driven by phase attenuation and its higher sensitivity to near-field effects. However, this threshold should be adjusted based on the noise level, especially when few receivers are used. The proposed criterion has been applied to the characterization of a real site in Italy, demonstrating that the inclusion of data affected by near-field effects leads to an overestimation of the shear wave damping ratio and significant variability in the estimated profiles.

Keywords

MASW, near-field effects, noise, shear-wave velocity, damping ratio

Introduction

Among the techniques for the *in situ* estimation of the shear-wave velocity V_S and damping ratio D_S, the Multichannel Analysis of Surface Waves (MASW) is becoming increasingly popular due to the cost-effectiveness and ease of use. Typical interpretation requires two main steps (e.g., Foti et al., 2014): (1) estimation of the propagation parameters of the surface waves (typically, Rayleigh or R-waves), i.e. dispersion and attenuation curves, which describe the

dependence of the phase velocity V_R and phase attenuation α_R on the frequency; (2) inversion of the experimental data to obtain profiles of V_S and D_S. It should be noted that the propagation of R-waves in linear viscoelastic media is described by a complex wavenumber, with the real part being linked to V_R and the imaginary part corresponding to α_R (e.g., Foti et al., 2014). Estimating V_R and α_R typically assumes only R-waves are present, but recorded data include both surface and body waves, causing near-field effects. This discrepancy typically leads to underestimation and/or oscillations in V_R at low frequencies (e.g., Zywicki and Rix, 2005; Rahimi et al., 2021). Recommendations to minimize near-field errors include adjustments in acquisition layout and processing, with criteria based on statistical tests (Strobbia and Foti, 2006) or wavelength-based normalized offsets (e.g., Tokimatsu, 1995; Yoon and Rix, 2009; Rahimi et al., 2022). However, most research focused on V_R, while few studies investigated α_R (e.g., Yoon, 2005), without reaching effective ways to reduce such effects for α_R.

This paper provides insight into the influence of near-field effects on the estimated R-wave parameters, with a focus on phase attenuation. For this purpose, several MASW surveys with different acquisition layouts are simulated. The synthetic dataset is also corrupted by incoherent noise to address the joint influence of body waves and signal quality. The second part describes an application to a real site, highlighting the consequences of the inclusion of data influenced by near-field effects on the estimated V_S and D_S profiles.

Synthetic wavefield

The synthetic wavefield (hereafter referred to as "SW") represents the response of a homogeneous half-space to a vertical harmonic force of unit amplitude applied to the free surface with a frequency of 5 Hz. The mechanical properties of the medium are the following: V_S is 336 m/s, D_S is equal to 0.015, the Poisson ratio is 0.33, the mass density is 2,000 kg/m^3, and the P-wave damping ratio is equal to D_S. Vertical displacements at the free surface were computed using the direct stiffness approach (Kausel and Roësset, 1981), as implemented in the EDT software (Schevenels et al., 2009). The wavefield is the combination of both body and Rayleigh waves. For simplicity, this study focuses only on the displacement field harmonics at 5 Hz (i.e., the excitation frequency). The selected frequency represents the lower bound of the typical range used in MASW testing. However, in homogeneous media, the specific frequency does not affect the body wave component, as this depends solely on the distance compared to the wavelength (Tokimatsu, 1995). The corresponding theoretical R-wave wavenumber k_t is 0.1 rad/m, and attenuation α_t is 0.0015 rad/m, as obtained from the solution of the Rayleigh eigenvalue problem.

A parametric study simulated the wavefield in various uniformly spaced sensor arrays to assess the impact of near-field effects on R-wave parameters. The geometry can be described by the number of sensors N, the inter-receiver spacing

Δx, and the offset between the source and the closest receiver x_1. N was assumed equal to 12, 24, 48, and 100; Δx was set as equal to 0.3 m, 0.5 m, 1 m, 1.5 m, 2 m, 2.5 m, 3 m, 5 m, 10 m, 15 m, 20 m, and 30 m; and x_1 was set as equal to 1, 3, and 5 times Δx. A total of 144 acquisition geometries were modeled, each of which described in terms of the Normalized Array Center Distance (NACD; Yoon and Rix, 2009). This quantity is defined as the ratio between the array center (i.e., the average between the sensors' distances from the source x_i) and the investigated R-wave wavelength λ_R (in this case, equal to 62.8 m):

$$NACD = \frac{1}{N} \frac{\sum_{i=1}^{N} x_i}{\lambda_R} \quad (1)$$

The NACD combines information about both the acquisition geometry and the target R-wave. It is effective in describing discrepancies due to near-field effects (Yoon and Rix, 2009). The investigated NACD ranges 0.1 and 15, that are typical values covered in MASW surveys and explored in past studies (e.g., Yoon and Rix, 2009; Rahimi et al., 2022).

Influence of body waves

For each acquisition setup, the synthetic data were processed with the CFDBFa algorithm (Aimar et al., 2024a), which is a transform-based approach for the combined estimation of V_R (or, alternatively, the wavenumber k_R) and α_R, including explicit modeling of the cylindric shape of the Rayleigh wavefront. To address the influence of body waves, we calculated the ratio between the estimated R-wave parameters (i.e., k_e and α_e) and the corresponding theoretical values (i.e., k_t and α_t; Yoon and Rix, 2009). Fig. 1 summarizes the results of the parametric analysis, showing the normalized wave parameters as a function of the NACD. The datapoints with a transparent layer correspond to rather short arrays compared to λ_R (i.e., NACD < 0.5), that are not typically used in MASW surveys due to the limited wavenumber resolution (Foti et al., 2002).

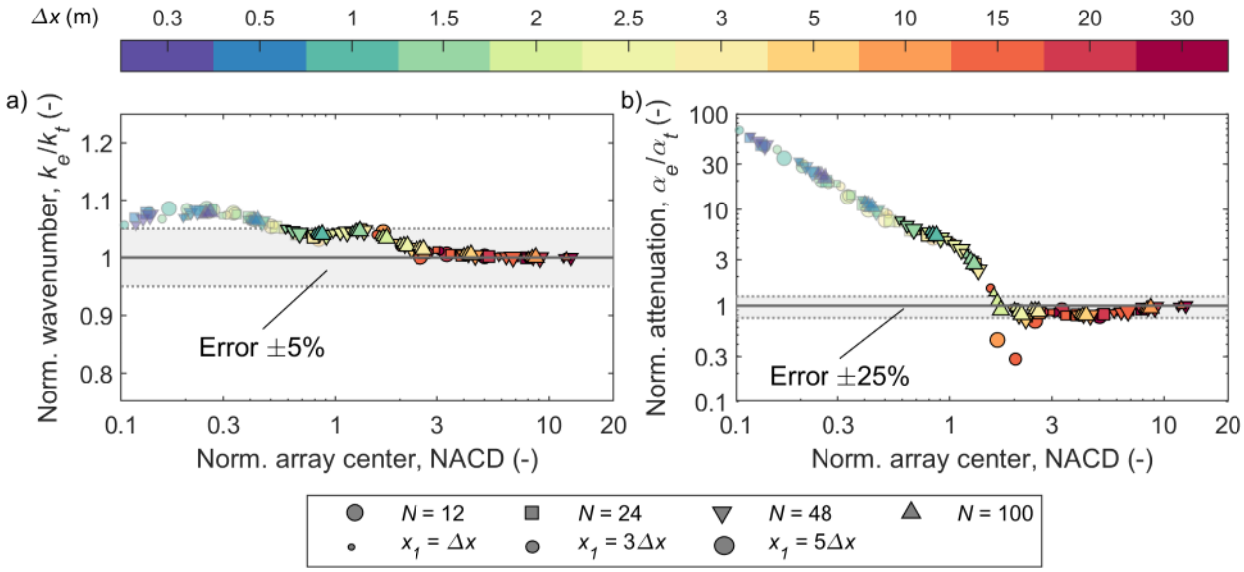

78

79 Fig. 1. Results of the parametric analysis on SW: a) k_e/k_t vs. NACD; b) α_e/α_t vs. NACD. Each data point corresponds to a
80 specific acquisition geometry, described in terms of N, Δx, and x_1. The horizontal bands correspond to an estimation
81 error of ±5% for k_R and of ±25% for α_R.

82

83 The CFDBFa provides reliable estimates of the wavenumber and the attenuation when the NACD is large, i.e., when the
84 acquisition is performed at large distances from the source. As for the wavenumber (Fig. 1a), it is slightly overpredicted
85 (hence, there is a small underestimation of V_R) as the NACD decreases, although the estimation error is less than 10%
86 and it becomes negligible (i.e., less than 5%) at NACD > 1-2. This behavior in the estimated V_R is a direct effect of body
87 waves, as confirmed by various in-situ observations (Yoon and Rix, 2009; Rahimi et al., 2021). Instead, the attenuation
88 is strongly overpredicted at short NACDs, with α_e being even 10-100 times larger than α_t. For this reason, the vertical
89 axis of Fig. 1b is plotted on a logarithmic scale. The error in α_e is relevant even at moderately large distances, and it
90 becomes less than 25% only at NACD > 2. Notably, the 25% threshold error for phase attenuation in Fig. 1b is larger than
91 that used for the wavenumber (5%; e.g., Yoon and Rix, 2009). This is due to the greater uncertainty associated with
92 phase attenuation compared to phase velocity, as well as its generally less influential role in the inversion process (e.g.,
93 Verachtert, 2018; Bergamo et al., 2023). Moreover, the 25% threshold represents a practical compromise between
94 estimation accuracy and the need to preserve low-frequency data, as further discussed in the "Discussion" section. Also,
95 α_e is quite sensitive to the number of sensors of the acquisition layout, with a higher tendency to drift when N is small.
96 There are two outliers with a significant underestimation of α_t around NACD = 1.5-2. A possible explanation could be
97 mutual interference between body waves and surface waves, which have comparable amplitudes in this distance-to-

wavelength range (e.g., Tokimatsu, 1995), leading to anomalous α_e values. However, this behavior only occurs for N = 12, which represents an acquisition setup less commonly used in ordinary near-surface site characterization. Other acquisition setups do not exhibit similar anomalies.

Influence of incoherent noise

The presence of incoherent noise was modeled through a Monte Carlo procedure, in which white Gaussian noise (e.g., O'Neill, 2003; Bergamo et al., 2023; Mukherjee et al., 2025) was added to SW to generate a new wavefield, hereafter labelled as "SW-n". Specifically, 50 independent realizations of white Gaussian noise were generated for each location and superimposed onto the original physics-based signal. This process resulted in 50 noisy signals at each simulated array. The amplitude of the noise signal was constant for all receivers of each simulated array and was calibrated so that the signal-to-noise ratio (SNR) at the farthest receiver was equal to 10 dB. This SNR is consistent with that commonly suggested for MASW testing (Wood and Cox, 2012; Foti et al., 2018). The waveform data were processed using the CFDBFa algorithm (Aimar et al., 2024a), obtaining a distribution of normalized wavenumber k_e/k_t and of normalized attenuation α_e/α_t, for each simulated array.

Fig. 2 reports the normalized wave parameters as a function of the NACD, in which the statistical distribution is synthetically described by a region centered at the median value and with an extent equal to the logarithmic standard deviation $\sigma_{\ln}$. Indeed, the variability of the estimated wave parameters due to incoherent noise can be modeled through a lognormal distribution (Aimar, 2022). In this case, different regions are defined to address the influence of the number of sensors N on k_e and α_e.

As for the wavenumber, there is a good degree of matching over the whole investigated NACD range. Besides, the variability is generally small (i.e., $\sigma_{\ln}$ less than 0.10). However, for rather small NACDs, the CFDBFa tends to underestimate it, differently from what is observed for the dataset SW. On the other hand, this anomaly occurs only at NACD < 0.3, which is not involved in the usual MASW testing (Foti et al., 2002).

Focusing on the attenuation, the distribution of α_e/α_t follows a trend consistent with the one obtained from the dataset SW (i.e., including only body waves). However, the variability is an order of magnitude larger than the corresponding $\sigma_{\ln}$ for k_e. Specifically, it tends to increase with the NACD, with a maximum at NACD = 1.5-2, exactly in correspondence with the transition region where the body waves start to become less relevant. Then, it decreases at larger NACDs. Notably, the trend of $\sigma_{\ln}$ is strongly dependent on N. Arrays with few receivers return more variable estimates of α_e, with $\sigma_{\ln}$ up to 1 at NACD = 2. Instead, using a large number of sensors (i.e., N = 48 or 100) allows the variability to decrease significantly, with $\sigma_{\ln}$ being now limited to 0.3.

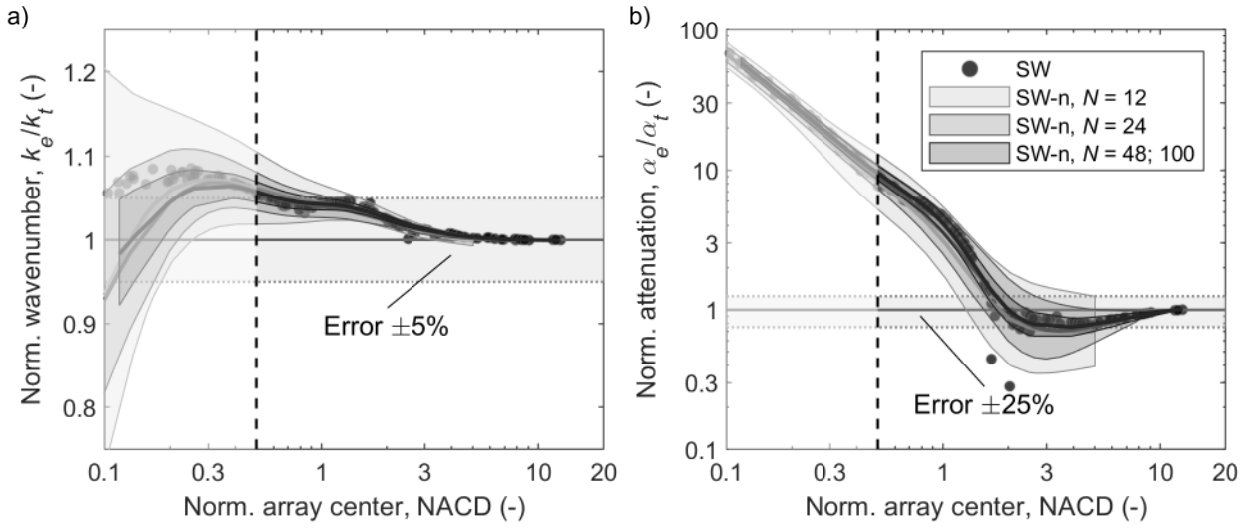

Fig. 2. Results of the parametric analysis on SW-n: a) k_e/k_t vs. NACD; b) α_e/α_t vs. NACD. The transparent layer at NACD < 0.5 highlights the region not typically used in MASW surveys due to the limited wavenumber resolution (Foti et al., 2002). The horizontal bands correspond to an estimation error of ±5% for k_R and of ±25% for α_R.

Discussion

The results for datasets SW and SW-n highlight that the influence of body waves (and of incoherent noise) is adequately mitigated for NACD ≥ 2-3, for both V_R and α_R. It should be noted that this NACD threshold is mostly dictated by the influence of near-field effects on α_R rather than on V_R. Indeed, the estimation error on V_R is negligible (quantitatively, less than 5%) for NACD > 1, consistently with the results of Yoon and Rix (2009) and Rahimi et al. (2022). On the other hand, for NACD ≥ 2-3, the estimation error for α_R is less than 20-25% on average. This error seems large, but a 10% error can be achieved only at NACDs larger than 8. This would imply the massive discarding of low-frequency data (with the consequent strong reduction of the investigated depth) and/or the need of using very long arrays with large spacing/number of receivers, which is not suitable for ordinary applications. Furthermore, arrays with fewer sensors are more sensitive to incoherent noise, as the variability of the estimates is larger. At NACD = 2-3, the statistical upper boundary of the error (corresponding to the median and one logarithmic standard deviation) can increase up to 35%, 50%, and 65%, for *N* equal to 48-100, 24 and 12, respectively. On the other hand, these variability estimates are obtained from synthetic data with the conservative (albeit realistic) assumption of SNR = 10dB at the farthest receiver. Indeed, many MASW surveys are characterized by larger SNR levels.

In summary, in the presence of a MASW survey, near-field effects on the estimated V_R and α_R can be mitigated by considering only those experimental data whose NACD exceeds 2-3.

Application on a real site

The proposed NACD criterion was applied for the interpretation of the MASW data collected at the Mirandola site (Italy) during the InterPACIFIC project (Garofalo et al., 2016b). This site is characterized by alternating layers of fine sands and clays, overlying a rock-like formation at depths between 50 m and 150 m (Garofalo et al., 2016a). Due to the complex stratigraphy, this site represents an appealing case study to gain preliminary insight into the effectiveness of the proposed NACD criterion. The site characterization involved two linear arrays of 48 vertical 4.5-Hz geophones, with Δx equal to 1 m and 2 m, respectively. In both cases, the wavefield was generated by a sledgehammer, with source point offsets of 2.5 m, 3 m, and 15 m. The experimental data were interpreted using the CFDBFa algorithm (Aimar et al., 2024a), over a frequency band between 2 Hz and 25 Hz, with a focus on the R-wave fundamental mode, which is dominant in this range.

Fig. 3 reports the estimated V_R and α_R versus frequency, showing data with NACD below or above the threshold NACD = 2 with different marker types. This threshold corresponds to the lower limit of the proposed NACD criterion (i.e., 2-3), being the data SNR larger than 20 in the frequency band of interest. Specifically, two data clusters are identified: (1) a set with all the data points, and (2) a subset with NACD ≥ 2, which should not be affected by near-field effects. These data clusters are labeled as "All data" and "NACD ≥ 2", respectively. For each cluster, the distribution of the experimental data is described by the median and the logarithmic standard deviation (σ_{lnV} and $\sigma_{ln\alpha}$, respectively), calculated over a set of log-spaced frequency bins, and it is represented through error bar plots. Besides, the data in Fig. 3a are overlaid onto the distribution of the V_R estimates for the Mirandola site reported in Garofalo et al. (2016b), represented in terms of intervals given by one logarithmic standard deviation around the median value and labelled as "Gea2016 - $\mu\pm\sigma$". This dataset is an effective benchmark for assessing the reliability of the V_R estimates, since it includes data from ambient noise measurements, which are unlikely to be affected by near-field effects.

As for V_R, the two trends of the experimental data are in good agreement, although the "All data" set is affected by a larger variability at low frequencies. Furthermore, this set shows noticeable deviations at low frequencies, sometimes underestimating and at other times overestimating the V_R reported in Garofalo et al. (2016b). Indeed, it is important to note that near-field effects may also cause overestimation of the theoretical V_R in layered media (e.g., Yoon and Rix, 2009). Conversely, both the individual data points and the statistical distribution of the "NACD ≥ 2" are consistent with Garofalo et al. (2016b), thus corroborating the validity of the proposed NACD threshold. As for α_R, the inclusion of all the data would induce a strong increase in the median α_R, with a clear drift from the "NACD ≥ 2" trend at frequencies below 7 Hz. Also, $\sigma_{ln\alpha}$ increases dramatically up to 1.0 for the "All data" set at low frequencies, while it ranges between

0.3-0.5 for the other dataset at all the frequencies. This difference is a consequence of the erratic distribution of the α_R data points at low frequencies in the "All data" set. This is a clear indication of the influence of body waves and of incoherent noise, that results in a dramatic increase in the α_R and $\sigma_{ln\alpha}$. On the other hand, their influence on V_R seems less relevant.

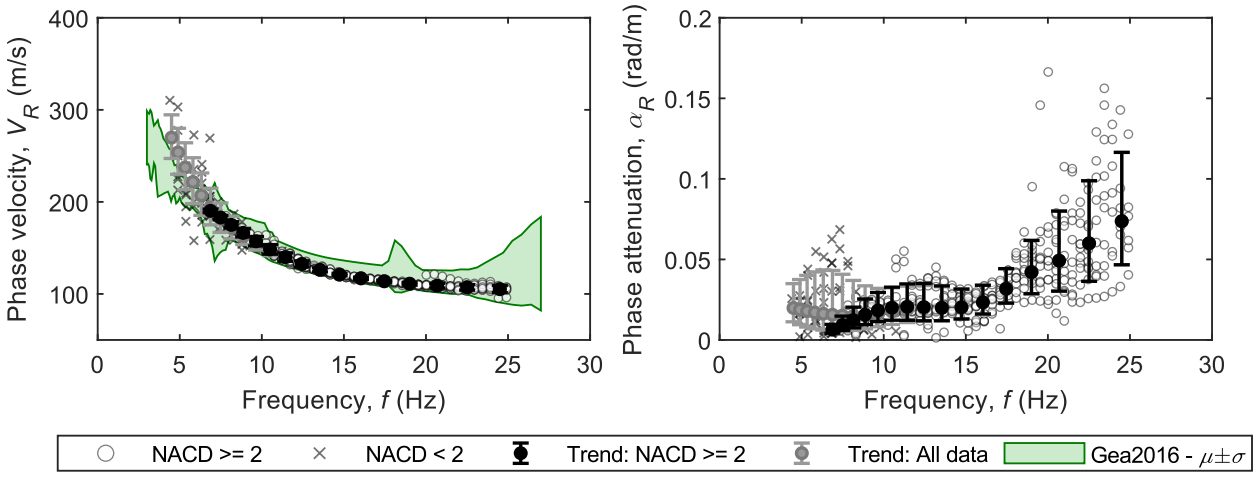

Fig. 3. Application of the proposed NACD criterion to the Mirandola dataset: a) Estimated V_R versus frequency; b) Estimated α_R versus frequency. The figure includes the distribution of the V_R estimates reported in Garofalo et al. (2016b), for comparison purposes.

Finally, an inversion of the two experimental datasets was performed to obtain the V_S and D_S profiles at the site. This provides insight into the consequences of an incorrect separation of near-field effects on V_S and D_S. The inversion was performed using a Monte Carlo joint inversion method (Aimar et al., 2024b). The inversion involved 10,000 trial ground models for each dataset, assuming a three-layer profile. The trial models covered a comprehensive range of layer thicknesses, V_S, and D_S values. Typical values of the mass density and the Poisson ratio were adopted, based on the available geological information (Foti et al., 2018), whereas the P-wave damping ratio was assumed as equal to D_S.

Fig. 4 represents the statistical distribution of the 10 best-fitting V_S and D_S profiles (i.e., those with the smallest deviation between the theoretical V_R and α_R versus frequency curves and the experimental ones), computed under the assumption of lognormal distribution for V_S and D_S (e.g., Schevenels, 2007; Li and Assimaki, 2010). Note that this representation does not provide a rigorous picture of model uncertainties, as it describes the variability of a subset of the collection of profiles consistent with the experimental data, and it assumes that the true model has three layers – hence, the uncertainty due to inversion parameterization is neglected. However, this simplified representation is used

to better understand the impact of near-field effects on the estimated ground models. Profiles of the "NACD ≥ 2" dataset are truncated at $z = \lambda_{max}/2 = 14$ m (with λ_{max} being the maximum experimental wavelength), which corresponds to the maximum investigable depth that can be achieved from the corresponding V_R data. The corresponding value for the "All data" dataset is $z = 26$ m; however, the depth axis is limited at $z = 20$ m because no layer interface was identified beneath it. Fig. S1 in the Electronic Supplement represents the resulting profiles, together with the comparison between the theoretical curves with the experimental ones, for both datasets. Besides, V_S profiles in Fig. 4a are compared with the median profiles obtained from the invasive and the non-invasive tests reported in Garofalo et al. (2016a), labelled as "Gea2016: Invasive" and "Gea2016: Non-invasive", respectively.

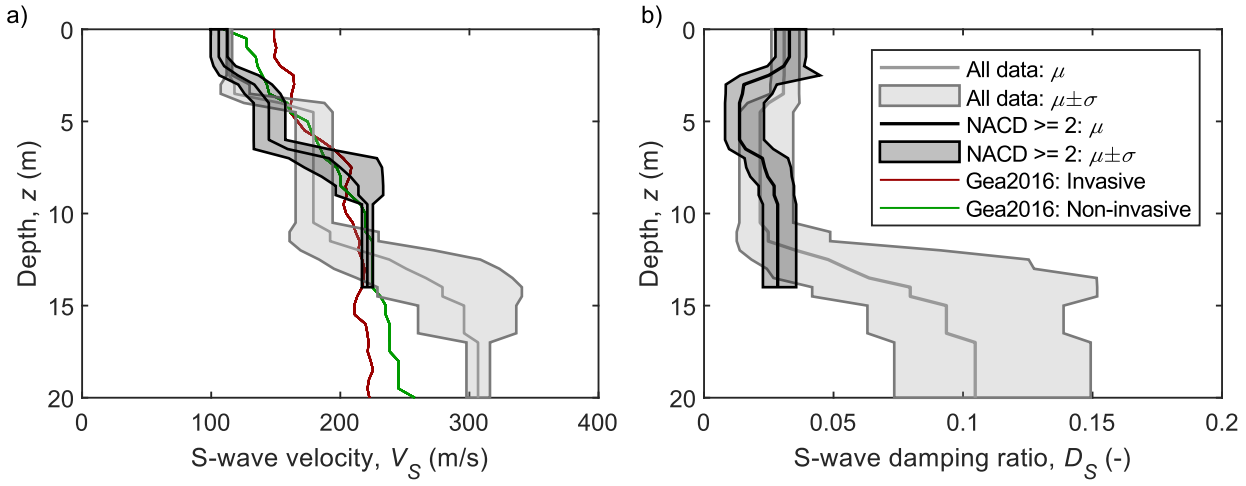

Fig. 4. Statistical distribution of a) V_S profiles and b) D_S profiles for the "All data" and "NACD ≥ 2" datasets. The regions indicate the interval defined by the median and one logarithmic standard deviation, at each depth. The figure includes median V_S profiles obtained from the invasive and the non-invasive tests reported in Garofalo et al. (2016a), for comparison purposes.

Fig. 4a shows a good match between the "NACD ≥ 2" dataset and the V_S profiles reported in Garofalo et al. (2016a), proving the reliability of the corresponding estimated profiles, especially at greater depths. As for D_S, the resulting profiles from the "All data" dataset show two main differences compared to those obtained from "NACD ≥ 2". On the one hand, the "All data" dataset results in a large D_S at depths larger than 10 m. Also, it increases up to 10-15% for depths larger than 15 m (i.e., beyond the maximum investigable depth of the "NACD ≥ 2" dataset), due to the large median α_R of the "All data" dataset at low frequencies. These estimates are rather large compared to the expected values for D_S of fine-grained soils, which typically range between 1% and 3% (e.g., Darendeli, 2001). This even

overestimates other effects such as wave scattering, as the corresponding "equivalent" damping ratio is generally around 1-3% (e.g., Wu, 1982; Kurita et al., 1996). Furthermore, the variability of the estimated D_S profiles is larger at z > 5 m, with even greater variability at deeper depths, since the "All data" dataset is affected by large variability in the experimental α_R at low frequencies. This partially prevents an effective constraint on the inverted profiles, resulting in highly scattered D_S profiles, whereas the "NACD ≥ 2" dataset gives a clear trend at all depths for both V_S and D_S.

Conclusions

This study investigated the influence of near-field effects and incoherent noise on the estimated R-wave phase velocity and phase attenuation from MASW tests. A parametric analysis over a synthetic surface wave dataset demonstrated that they induce a slight underestimation of the phase velocity, whereas the phase attenuation is strongly overestimated for small NACD values. Furthermore, the data variability induced by incoherent noise is large when the spatial sampling density is reduced. However, near-field effects can be mitigated by selecting experimental data with NACD larger than 2-3. The proposed criterion has been applied for the characterization of the Mirandola site in Italy, highlighting that the inclusion of data affected by near-field effects leads to a significant increase in the estimated damping ratio and its variability at large depths.

This study demonstrated the higher sensitivity of phase attenuation to body waves and incoherent noise compared to phase velocity. Therefore, a more conservative NACD threshold should be enforced for the joint estimation of S-wave velocity and damping ratio, compared to previous studies that focused only on soil stiffness characterization. The proposed threshold of NACD = 2-3 can be considered as a good guideline, although further studies are needed to understand the impact of near-field effects on layered media with complex wave patterns (e.g., higher modes) and different noise scenarios. These findings will contribute to a robust estimation of soil dissipation parameters at large depths.

Acknowledgements

This research has been partially funded by the Italian Civil Protection Agency under the framework of the ReLUIS project.

Data availability

Synthetic data will be made available upon request. Data at the Mirandola site were extracted from the InterPacific Project and are available at http://interpacific.geopsy.org/.

Supplemental Materials

Fig. S1 is available online in the ASCE Library (ascelibrary.org).

References

247 Aimar (2022) Uncertainties in the estimation of the shear-wave velocity and the small-strain damping ratio from surface
248 wave analysis, PhD thesis, Politecnico di Torino.
249 Aimar, Foti, Cox (2024a) Novel techniques for in situ estimation of shear-wave velocity and damping ratio through
250 MASW testing – I: a beamforming procedure for extracting Rayleigh-wave phase velocity and phase attenuation,
251 Geophys. J. Int., 237: 506-524.
252 Aimar, Foti, Cox (2024b) Novel techniques for in situ estimation of shear-wave velocity and damping ratio through
253 MASW testing part II: a Monte Carlo algorithm for the joint inversion of phase velocity and phase attenuation, Geophys.
254 J. Int., 237: 525-539.
255 Bergamo, Maranò, Fäh (2023) Joint estimation of s-wave velocity and damping ratio of the near-surface from active
256 Rayleigh wave surveys processed with a Wavefield decomposition approach, Geophys. J. Int., 233: 1560-1579.
257 Darendeli (2001) Development of a new family of normalized modulus reduction and material damping curves, PhD
258 thesis, University of Texas at Austin.
259 Foti, Hollender, Garofalo, Albarello, Asten, Bard, Comina, Cornou, Cox, Di Giulio, Forbriger, Hayashi, Lunedei, Martin,
260 Mercerat, Ohrnberger, Poggi, Renalier, Sicilia, Socco (2018) Guidelines for the good practice of surface wave analysis: a
261 product of the InterPACIFIC project, Bull. Earthq. Eng., 16: 2367-2420.
262 Foti, Lai, Rix, Strobbia. 2014. Surface wave methods for near-surface site characterization (CRC press).
263 Foti, Sambuelli, Socco, Strobbia. (2002) Spatial sampling issues in fk analysis of surface waves. In 15th EEGS Symposium
264 on the Application of Geophysics to Engineering and Environmental Problems. European Association of Geoscientists &
265 Engineers.
266 Garofalo, Foti, Hollender, Bard, Cornou, Cox, Dechamp, Ohrnberger, Perron, Sicilia, Teague, Vergniault (2016a)
267 InterPACIFIC project: Comparison of invasive and non-invasive methods for seismic site characterization. Part II: Inter-
268 comparison between surface-wave and borehole methods, Soil Dynam. Earth. Eng., 82: 241-254.
269 Garofalo, Foti, Hollender, Bard, Cornou, Cox, Ohrnberger, Sicilia, Asten, Di Giulio (2016b) InterPACIFIC project:
270 Comparison of invasive and non-invasive methods for seismic site characterization. Part I: Intra-comparison of surface
271 wave methods, Soil Dynam. Earth. Eng., 82: 222-240.
272 Kausel, Roësset (1981) Stiffness matrices for layered soils, Bull. Seismol. Soc. Am., 71: 1743-1761.
273 Kurita, Tsuzuki, Annaka, Shimada, Fujitani. (1996) Scattering attenuation of seismic waves in inhomogeneous media. In
274 Eleventh World Conference on Earthquake Engineering (11th WCEE). Elsevier Science Ltd.

Li, Assimaki (2010) Site-and motion-dependent parametric uncertainty of site-response analyses in earthquake simulations, Bull. Seismol. Soc. Am., 100: 954-968.

Mukherjee, Bhaumik, Naskar (2025) Modified S-transform based high-resolution dispersion imaging method for multi-channel surface wave data, 192: 109284.

O'Neill (2003) Full-waveform reflectivity for modelling, inversion and appraisal of seismic surface wave dispersion in shallow site investigations, University of Western Australia.

Rahimi, Wood, Himel (2022) Practical guidelines for near-field mitigation on array-based active surface wave testing, Geophys J Int, 229: 1531-1549.

Rahimi, Wood, Teague (2021) Performance of different transformation techniques for MASW data processing considering various site conditions, near-field effects, and modal separation, Surv. Geophys., 42: 1197-1225.

Schevenels (2007) The impact of uncertain dynamic soil characteristics on the prediction of ground vibrations, PhD thesis, KU Leuven.

Schevenels, Degrande, François (2009) EDT: an elastodynamics toolbox for MATLAB, Comput. Geosci.

Strobbia, Foti (2006) Multi-offset phase analysis of surface wave data (MOPA), J Appl Geophys, 59: 300-313.

Tokimatsu. (1995) Geotechnical site characterization using surface waves. In 1st International Conference on Earthquake Geotechnical Engineering, 1333-1368. Tokyo, Japan: Balkema.

Verachtert (2018) Deterministic and probabilistic determination of dynamic soil characteristics, PhD thesis, KU Leuven.

Wood, Cox. (2012) A comparison of MASW dispersion uncertainty and bias for impact and harmonic sources. In GeoCongress 2012: State of the Art and Practice in Geotechnical Engineering, 2756-2765.

Wu (1982) Attenuation of short period seismic waves due to scattering, Geophys. Res. Lett., 9: 9-12.

Yoon (2005) Array-based measurements of surface wave dispersion and attenuation using frequency-wavenumber analysis, PhD thesis, Georgia Institute of Technology.

Yoon, Rix (2009) Near-field effects on array-based surface wave methods with active sources, J Geotech Geoenviron Eng, 135.

Zywicki, Rix (2005) Mitigation of Near-Field Effects for Seismic Surface Wave Velocity Estimation with Cylindrical Beamformers, J. Geotech. Geoenviron. Eng., 131: 970-977.

Electronic Supplement to "Near-field effects on the in-situ estimation of shear-wave velocity and damping ratio from MASW tests"

Mauro Aimar and Sebastiano Foti

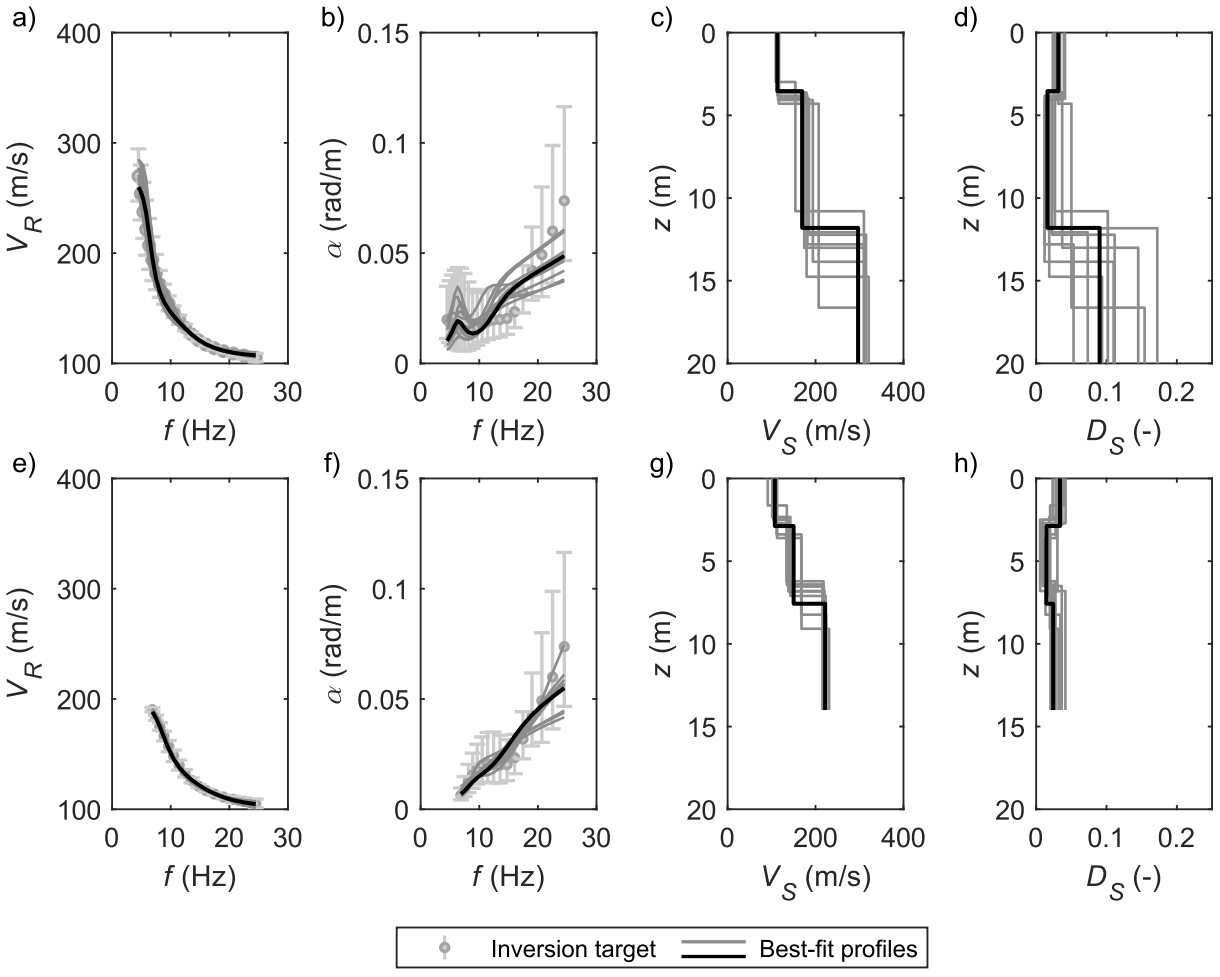

Fig. S1. Best fitting ground models to the "All data" (top row) and "NACD ≥ 2" (bottom row) datasets. Each row shows the comparison between theoretical vs. experimental data, for the phase velocity V_R (a and e) and phase attenuation α_R (b and f); the resulting S-wave velocity V_S (c and g) and damping ratio D_S (d and h) profiles. The black line represents the best-fit model (that is, the one with the smallest difference between theoretical and experimental V_R and α_R, as a reference. Profiles of the "NACD ≥ 2" dataset are truncated at $z = \lambda_{max}/2 = 14$ m (with λ_{max} being the maximum experimental wavelength), which corresponds to the maximum investigable depth that can be achieved from the corresponding V_R data. The corresponding value for the "All data" dataset is $z = 26$ m; however, the depth axis is limited at $z = 20$ m because no layer interface was identified beneath it.